Measurement of the complete nuclide production and kinetic energies of the system ^{136}Xe+hydrogen at 1 GeV per nucleon

P. Napolitani,[1,2,*] K.-H. Schmidt,[1] L. Tassan-Got,[2] P. Armbruster,[1] T. Enqvist,[1,†] A. Heinz,[1,3] V. Henzl,[1,‡] D. Henzlova,[1,§] A. Kelić,[1] R. Pleskač,[1] M. V. Ricciardi,[1] C. Schmitt,[1,§] O. Yordanov,[1] L. Audouin,[2] M. Bernas,[2] A. Lafriaskh,[2] F. Rejmund,[2,4] C. Stéphan,[2] J. Benlliure,[5] E. Casarejos,[5] M. Fernandez Ordonez,[5] J. Pereira,[5,‡] A. Boudard,[6] B. Fernandez,[6] S. Leray,[6] C. Villagrasa,[6,‖] and C. Volant[6]

[1]*GSI, Planckstr. 1, D-64291 Darmstadt, Germany*

[2]*IPN Orsay, Université Paris-Sud 11, CNRS/IN2P3, F-91406 Orsay cedex, France*

[3]*A.W. Wright Nuclear Structure Laboratory, Yale University, New Haven, Connecticut 06511, USA*

[4]*GANIL, CEA/DSM-CNRS/IN2P3, BP 55027, F-14076 Caen cedex 5, France*

[5]*Univ. de Santiago de Compostela, S-15782 S. de Compostela, Spain*

[6]*DAPNIA/SPhN, DSM-CEA, F-91191 Gif-sur-Yvette cedex, France*

(Received 5 June 2007; revised manuscript received 19 October 2007; published 26 December 2007)

We present an extensive overview of production cross sections and kinetic energies for the complete set of nuclides formed in the spallation of ^{136}Xe by protons at the incident energy of 1 GeV per nucleon. The measurement was performed in inverse kinematics at the GSI fragment separator. Slightly below the Businaro-Gallone point, ^{136}Xe is the stable nuclide with the largest neutron excess. The kinematic data and cross sections collected in this work for the full nuclide production are a general benchmark for modeling the spallation process in a neutron-rich nuclear system, where fission is characterized by predominantly mass-asymmetric splits.

DOI: 10.1103/PhysRevC.76.064609 PACS number(s): 25.40.Sc, 29.30.−h, 21.10.Gv, 25.60.Dz

I. INTRODUCTION

In recent years, a vast experimental campaign has been dedicated to the measurement of spallation reactions at relativistic energies at the GSI fragment separator [1]. The installation of a target of liquid hydrogen or deuterium [2] and the achromatic magnetic spectrometer [3] adapted to inverse-kinematics experiments were the tools for collecting high-resolution momentum measurements and extracting production cross sections for each residue, identified in mass and nuclear charge. Several systems, either favored for unveiling new physical aspects or directly relevant to applications, were studied. In spallation reactions, a large amount of the cross section which does not result in fission fragments results in the production of heavy nuclides; these heavy residues are, on average and almost independently of the neutron enrichment of the projectile, less neutron-rich than β-stable nuclides. This property makes neutron-rich nuclei an ideal spallation target for conceiving high-intensity neutron sources. Systems such as $^{197}\mathrm{Au}_{(800A\ \mathrm{MeV})}+p$ [4,5], $^{208}\mathrm{Pb}_{(500A\ \mathrm{MeV})}+p$ [6,7], $^{208}\mathrm{Pb}_{(1A\ \mathrm{GeV})}+p$ [8,9], $^{208}\mathrm{Pb}_{(1A\ \mathrm{GeV})}+d$ [10], $^{238}\mathrm{U}_{(1A\ \mathrm{GeV})}+p$ [11–15], and $^{238}\mathrm{U}_{(1A\ \mathrm{GeV})}+d$ [16,17] were measured to study sequential evaporation and its intricate competition with fission. The measurement of ^{56}Fe+p at various energies [18,19] focused the attention on systems below the Businaro-Gallone point [20,21] in the fissility region where the saddle point becomes unstable toward asymmetric splits, and revived the discussion on the intermediate-mass-fragment formation in spallation.

Twenty years ago, experiments in direct kinematics [22–29] focused on the contribution of this process in spallation; the corresponding phenomenological discussions [30–34] suggested interpretations beyond the general fission-evaporation picture [35,36] and in line with the onset of multifragmentation (reviews on this process can be found in Ref. [37]; Ref. [38] reviews ISIS (Indiana Silicon Sphere) experiments induced by high-energy protons). A specific analysis of kinematic features connected to the intermediate-mass fragment formation in the $^{56}\mathrm{Fe}_{(1A\ \mathrm{GeV})}+p$ system [18] and in the much heavier system $^{238}\mathrm{U}_{(1A\ \mathrm{GeV})}+p$ [14] pointed out the difficulty of connecting this process exclusively to fission. In the former system, the presence of multifragmentation was proposed as a relevant contribution. In the latter, the intermediate-mass-fragment formation was interpreted as fission events characterized by asymmetric splits, although surprisingly high fission velocities were observed. The modeling of the spallation reaction at relativistic incident energy depends largely on the degree of understanding of such a process.

In this respect, the measurement of an intermediate system was required to complete the survey on intermediate-mass-fragment formation. A new experiment was dedicated to the measurement of the complete residue production and the kinematics of the reaction $^{136}\mathrm{Xe}_{(1A\ \mathrm{GeV})}+p$. ^{136}Xe is the stable nuclide with the largest neutron excess $N-Z$, with a fissility below the Businaro-Gallone point. It is therefore best suited for studying simultaneously the process of intermediate-mass-fragment formation over a large range of light masses and

*Present address: LPC Caen, ENSICAEN, Université de Caen, CNRS/IN2P3, F-14050 Caen cedex 4, France.

†Present address: CUPP project, P.O. Box 22, 86801 Pyhäsalmi, Finland.

‡Present address: NSCL, Michigan State University, East Lansing, Michigan 48824, USA.

§Present address: IPN Lyon, Université de Lyon, CNRS/IN2P3, F-69622 Villeurbanne cedex, France.

‖Present address: IRSN, BP17, F-92262 Fontenay-aux-Roses cedex, France.

the production of heavy evaporation residues from a system which has a neutron-to-proton ratio N/Z close to lead on the one hand, and in a fissility region where symmetric splits have low probability on the other hand.

After a description of the experimental procedure, we present the measured cross sections for the production of fully identified nuclides formed in the reaction and the measured kinetic energies as a function of the mass of the residues. The compilation of cross sections and kinetic energies collected in the present work is the first to contain a large experimental survey on intermediate-mass-fragment production which extends to the heavy-residue production in a system where fission is characterized by predominantly mass-asymmetric splits.

II. EXPERIMENTAL PROCEDURE

The fragments were produced in inverse kinematics by directing a primary beam of ^{136}Xe at 1A GeV on a target of liquid hydrogen contained in a cryostat with thin titanium windows (see Table I). The projectile residues were then analyzed in-flight, using the inclusive measurement of their momenta along the beam axis. The placement of the detectors in the fragment separator for this experiment is sketched in Fig. 1. In the target area, a beam-current monitor was placed to measure the primary-beam intensity. The positions where the trajectories of the fragments intersect the dispersive focal plane (x_{DFP}) and the terminal focal plane (x_{TFP}) were registered by two scintillation detectors with a width of 200 mm and sensitive to the horizontal position. Their combined signals provided also the measurement of the time of flight. The fragments of ^{136}Xe, which at relativistic incident energies are fully stripped with high probability, were identified in nuclear charge Z by two ionization chambers placed in front of the terminal focal plane.

The primary beam interacted not only with the hydrogen contained in the cryostat but also with the cryostat itself, wrapped into insulating Mylar foils, and with the other layers of matter present in the target area, such as the beam-current monitor and the accelerator vacuum window. To measure the contribution of nonhydrogen target nuclei, the experiment was repeated under equal conditions, by replacing the liquid hydrogen target with an identical empty sample. Table I lists the compositions and thicknesses of all layers of matter placed in the beam line during the experiment.

TABLE I. List of layers interposed along the beam line in the target area and in the dispersive-plane region.

		Material Thickness (mg/cm^2)
Target area:		
Vacuum window	Ti	4.5
Beam-current monitor	Ti	13.5
Mylar foils	$C_5H_4O_2$	4.15
Front target windows	Ti	18.15
Liquid hydrogen	H_2	87.3
Rear target windows	Ti	18.15
Mylar foils	$C_5H_4O_2$	4.15[a]
Dispersive plane:		
Scintillator	C_9H_{10}	475.45 (C)+44.025 (H)
Degrader (wedges)	Al	816.6[b]

[a]Mylar is coated with 0.1 mg/cm^2 of aluminum.
[b]For the reference trajectory.

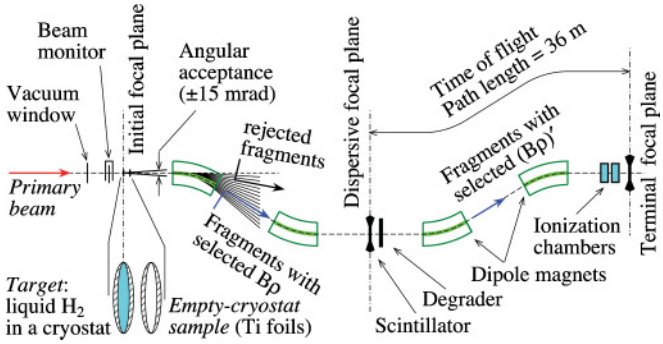

FIG. 1. (Color online) Layout of the GSI fragment separator. The positions of the four dipole magnets, the focal planes and the main detectors are shown in a horizontal plane view, to scale along the beam direction. The limited angular acceptance of ≈15 mrad in the laboratory frame is indicated.

A. High-resolution achromatic mode

In essence, the magnetic configuration of the spectrometer is based on four bending sections delimited by an initial focal plane, where the target is placed, and a terminal focal plane. The first pair of bending magnets and the second pair, with average magnetic fields B and B', respectively, constitute two portions of the spectrometer with opposite dispersion factors. The spectrometer has maximum dispersion in the center of the dispersive focal plane (x_{DFP}) and was set to be achromatic. More precisely, x_{DFP} is related to the momentum deviations $\delta p = (p - p_0)/p_0$ with respect to the reference trajectory p_0 in the first dispersive section and $\delta p'$ in the second dispersive section by

$$D\delta p + g x_{\mathrm{IFP}} = x_{\mathrm{DFP}} = D'\delta p' + g' x_{\mathrm{TFP}}, \qquad (1)$$

where x_{IFP} and x_{TFP} are the displacements in the initial and terminal focal plane, respectively, from a reference trajectory which, for convenience, was chosen to intersect all focal planes in their centers. D and D' are dispersion constants; g and g' are the magnification factors measured when moving from the extremes of the beam line toward the dispersive focal plane. The three optical parameters D, D', and g' were measured with uncertainties of 0.7%, 2.7%, and 1%, respectively, in an initial calibration run and later kept fixed to constant values for the whole experiment. We did not need to measure g as the beam hits the target in the center of the initial focal plane. As Eq. (1) shows, the momentum deviation of the fragments is completely defined by the displacements x_{DFP} and x_{TFP}, which were measured by placing a scintillator detector in each of the corresponding focal planes. By substituting the momentum deviation δp by the magnetic-rigidity deviation

$\delta(B\rho) = (B\rho - B\rho_0)/B\rho_0$ with respect to the reference trajectory $B\rho_0$, Eq. (1) leads to the two equations that govern the data analysis:

$$B\rho = B\rho_0 \left(1 + \frac{x_{\mathrm{DFP}}}{D}\right), \tag{2}$$

$$(B\rho)' = B'\rho_0' \left(1 + \frac{x_{\mathrm{DFP}} - g' x_{\mathrm{TFP}}}{D'}\right). \tag{3}$$

The curvature radii ρ_0 and ρ_0' were kept fixed for the whole experimental run. To scan the full distribution of magnetic rigidities of the fragments, the magnetic fields B and B' had to be changed several times due to the limited acceptance in magnetic rigidity, which selects ranges of around 3% for each individual magnetic setting (B, B') in the dispersive focal plane. To keep all the optical parameters strictly unchanged, the magnetic fields of the ensemble of magnets were scaled by equal factors for the first and the second dispersive section, respectively. These two factors should differ slightly to keep the range of elements selected by the spectrometer fixed for a set of measurements.

B. Separation of fragments

As the time of flight could be measured between the dispersive and the terminal focal planes, we could associate a mass-to-charge ratio A/Z to each fragment having magnetic rigidity $(B\rho)'$ in the second dispersive section, that is,

$$\frac{A}{Z} = \frac{1}{c}\frac{e}{m_0 + \delta m}\frac{(B\rho)'}{(\beta\gamma)'}, \tag{4}$$

where c is the velocity of light, e the electron charge magnitude, m_0 the nuclear mass unit, $\delta m = \mathrm{d}M/A$ the mass excess per nucleon, and $\beta\gamma$ the relativistic factor, which is determined in the laboratory frame in longitudinal direction.

Due to the limited acceptance in magnetic rigidity, the scanning of the whole A/Z distribution of fragments required several magnetic-field scalings. When thick layers of matter are inserted between the two dispersive sections, the fragments lose part of their kinetic energy as a quadratic function of the charge, and their magnetic rigidities change. This property can be exploited [39]: it imposes a charge selection in the second dispersive section which can be employed to measure restricted groups of elements. For this purpose, we used an aluminum layer (degrader) of 816.6 mg/cm^2 in the beam line and selected three bands of nuclides centered around silver, zinc, and aluminum, according to the expectation that the production yields do not vary largely within each single band. The aluminum degrader was shaped so as to not perturb the achromatic mode.

III. ANALYSIS

The first step of the analysis consisted of identifying each fragment in nuclear charge Z by calibrating the ionization chambers and in mass A from the magnetic rigidity and the time-of-flight measurement of their momentum in the second dispersive section of the spectrometer. Afterward, from the knowledge of the A/Z ratio and the magnetic rigidity measured in the first dispersive section of the spectrometer, the momentum was deduced a second time with higher precision than from the time-of-flight measurement. Hence, a high-resolution distribution of longitudinal recoil velocities in the projectile frame $v_{\parallel}^{b}$ was associated with each reaction product identified in nuclear mass and charge. These distributions were normalized to the beam dose per target thickness, and the parasitic effect of the reactions in layers differing from hydrogen was removed, so that the integral of the distribution was equal to the measured production yield I for each nuclide. The analysis then focused on the shape of these spectra which, without a dedicated analysis procedure, were still not directly suited for extracting the physical quantities related to the kinematics and the production of the reaction. To reconstruct the full distribution of emission velocities, independent of the experimental conditions, the geometry of the angular acceptance of the spectrometer was accurately accounted for. This reconstruction was necessary for extracting the production yield of each nuclide as well as the kinetic-energy distributions. Finally, the formation cross section σ for each primary reaction product was extracted from the production yield by accounting for the secondary reactions induced by the primary fragments in the hydrogen target and in the dispersive plane, where a scintillator detector and a degrader were placed.

A. Nuclide identification

The relativistic factor β in Eq. (4) is the ratio $\beta = \ell/ct$, where ℓ is the path length, which is given by $\ell_0 = 36$ m for a fragment centered at all focal planes, and t is the actual time of flight. t could not be deduced directly from the measured time of flight t' because of nonlinear effects of the light-propagation time in the scintillating detectors (resulting into quadratic terms in the path x_{DFP} and x_{TFP}) and an amplitude dependence on the charge of the signal. To extract the actual values of ℓ and t, a set of eight coefficients k_i, was introduced in the form

$$\ell = \ell_0 + k_1 x_{\mathrm{DFP}} + k_2 x_{\mathrm{TFP}}, \tag{5}$$

$$t = k_3 + k_4 t' + k_5 x_{\mathrm{DFP}}^2 + k_6 x_{\mathrm{TFP}}^2 + k_7 e^{-k_8 Z^2}. \tag{6}$$

The terms k_i were deduced by numerical optimization and used for the whole data analysis.

The full nuclide identification was obtained from Eqs. (3) and (4). The raw data are shown in Fig. 2, where all the events collected in the experiment are shown as a nuclide identification plot.

B. Beam dose per target thickness

The number of events registered in different settings of the separator magnets were normalized to the same beam dose in order to have consistent weights. The normalized counts $N(i)$, registered for an individual experimental run i, determined by a specific magnetic setting, are obtained by dividing the number of events $n(i)$ by four coefficients, that is,

$$N(i) = \frac{n(i)}{a_b f_b(i)[1 - \tau(i)]\alpha_{\mathrm{H}_2}}, \tag{7}$$

where a_b is a coefficient to convert the secondary-electron current produced by the primary beam into the number of projectiles impinging on the target, $f_b(i)$ is a measurement of the primary-beam current by the beam-current monitor [40],

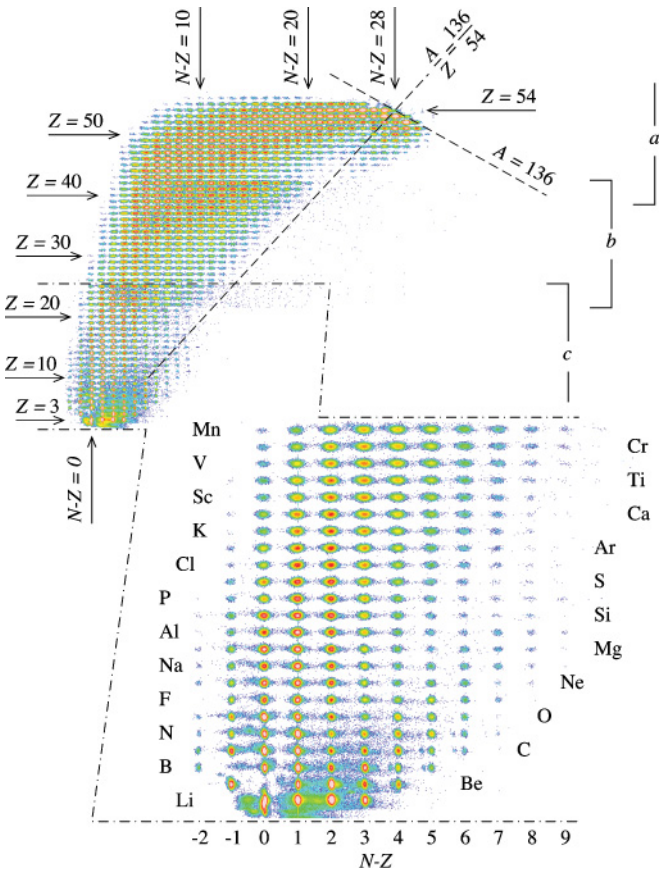

FIG. 2. (Color online) Ensemble of all events, identified in nuclear charge and mass. The overlapping bands a, b, and c correspond to the three groups of magnetic settings for nuclide distributions centered around ^{120}Ag, ^{69}Zn, and ^{24}Al, respectively. The band c, corresponding to light nuclides, is enlarged to emphasize the quality of the isotopic resolution.

$\tau(i)$ is the measured fractional dead time of the data acquisition system, and α_{H_2} is the number of nuclei per area of the liquid hydrogen.

In a dedicated experiment, the spill structure was digitized by both the beam-current monitor and the scintillation detector, as shown in the inset of Fig. 3; the comparison of the two spectra fixed the coefficient a_b, according to the method described in Ref. [41]. After accurately subtracting the offset of the beam-current monitor and integrating the recorded counts over each spill, a quadratic dependence of the particle counting as a function of the beam intensity was obtained due to the saturation of the scintillation detector, as shown in the inset of Fig. 3. The coefficient a_b was deduced as the initial slope of the function, with an uncertainty of 1%. In a previous experiment [42] a slight dependence of this coefficient with the position of the beam spot on the target (which has a fluctuation of the order of 1 mm) was estimated to introduce an additional uncertainty of around 5%, which we apply to the present data.

C. Longitudinal recoil velocities

Once a fragment is identified in mass and charge, its velocity is directly obtained from the magnetic rigidity. As no further

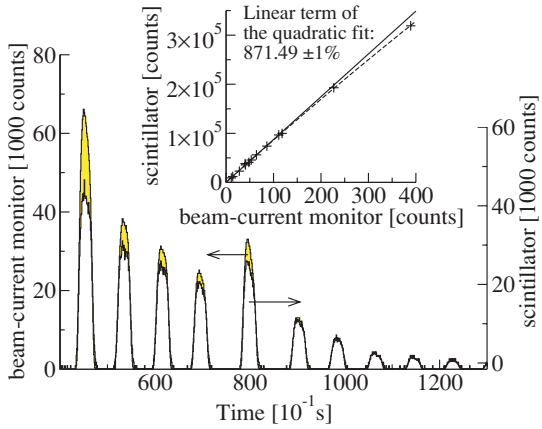

FIG. 3. (Color online) Beam-current monitor calibration. Superposition of counts in the beam-monitor (colored spectrum, axis label on the left) and counts in the scintillator (white-filled spectrum, axis label on the right). The beam-monitor spectrum is multiplied by the parameter a_b, which coincides with the calibration slope (solid line) shown in the inset.

layer of matter was present behind the target in the whole first dispersive section of the spectrometer, the relativistic factor $\beta\gamma$ in the laboratory frame in the longitudinal direction could be deduced more precisely from the magnetic rigidity $B\rho$, defined in Eq. (2), rather than from $(B\rho)'$, defined in Eq. (3), so that

$$(\beta\gamma)_{\parallel}^{L} = B\rho\,\frac{1}{c}\,\frac{e}{m_0+\delta m}\,\frac{Z}{A}. \tag{8}$$

To change from the $(\beta\gamma)_{\parallel}^{L}$ factor in the laboratory frame to the longitudinal velocity $v_{\parallel}^{b}$ in the beam frame, the energy loss in the target was taken into account. In particular, we assumed that the average position where the collision occurs corresponds to half of the total thickness of the ensemble of layers present in the target area (listed in Table I). We defined the beam frame in correspondence with the velocity of the projectile at this position. The high precision in deducing recoil velocities for individual reaction products is given by the measurement of $B\rho$ [or $(\beta\gamma)_{\parallel}^{L}$], which has a relative uncertainty of only 5×10^{-4} (FWHM). However, to access the reaction kinematics, the details of the shape of the longitudinal-velocity distribution $dN(v_{\parallel}^{b})/dv_{\parallel}^{b}$ had to be examined for each nuclide.

In Sec. II we explained that the spectrometer has a limited acceptance in momentum; for this reason, the full longitudinal momentum distribution for a single nuclide was constructed by composing several measurements with different magnetic settings. The spectrometer has also a limited acceptance for the emission angles so that it can be demonstrated that the measured spectra for intermediate-mass fragments are close to invariant cross sections [18]. Another technical difficulty was the contribution to the spectrum $dN(v_{\parallel}^{b})/dv_{\parallel}^{b}$ of reactions occurring in any layer of the target area other than liquid hydrogen. To solve this problem, all experimental steps were repeated under equal conditions with an empty-target sample in order to deduce the longitudinal-velocity distribution $dN'(v_{\parallel}^{b})/dv_{\parallel}^{b}$ related to parasitic reactions in all layers other

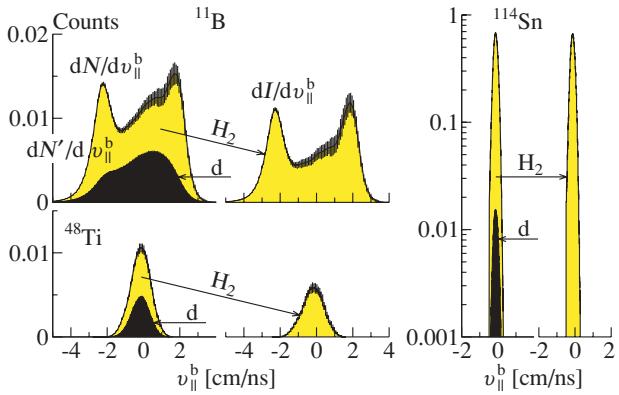

FIG. 4. (Color online) Subtraction of the contribution of nonhydrogen target nuclei (label "d", for "dummy") to obtain the measured velocity distributions for ^{11}B, ^{48}Ti, and ^{114}Sn. The left spectra represent the full measured contribution to the velocity distribution associated with the hydrogen target (color-filled histograms) and to nonhydrogen target nuclei (black-filled histograms), while the right spectra represent the deduced hydrogen contribution alone. The contribution from the windows is large for light fragments (^{11}B, ^{48}Ti) and negligible for heavy residues (^{114}Sn).

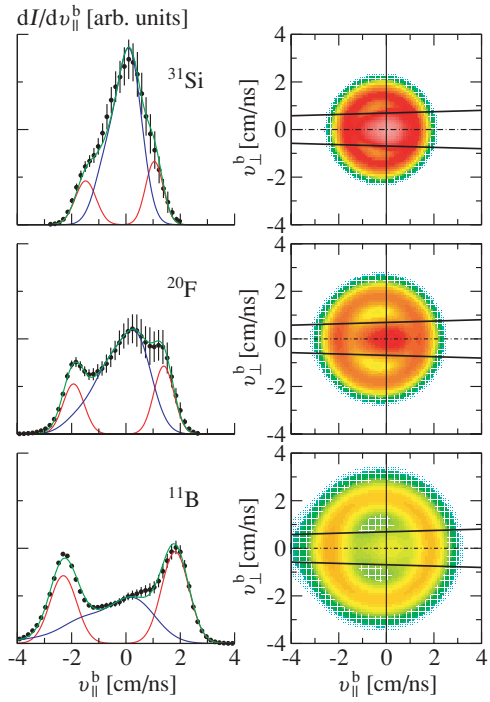

FIG. 5. (Color online) Left column: Measured velocity distributions for three nuclides, ^{11}B, ^{20}F, ^{31}Si. All spectra are normalized to the same integral value. The spectra are fitted (green curves) in order to determine the concave (red curves) and the convex (blue curves) components; see text. Right column: Planar cuts along the beam axis of the reconstructed velocity-space distribution $d\sigma/d\boldsymbol{v}^b$ in the beam frame. All distributions, reconstructed from the corresponding measured velocity distributions, are normalized to the same integral value and described by a logarithmic evolution of the color, where the span from blue to pale red corresponds to a factor of 2 in the intensity. The two lines indicate the boundaries of the angular acceptance, inside of which the fragments could be measured.

than hydrogen present in the target area (listed in Table I). The measured distribution of yields $dI(v_\parallel^b)/dv_\parallel^b$ was directly obtained as the difference between the two distributions $dN(v_\parallel^b)/dv_\parallel^b$ and $dN'(v_\parallel^b)/dv_\parallel^b$, both normalized to the number of nuclei per area of liquid hydrogen α_{H_2}.

It should be remarked that while the parasitic layers of matter were designed to be as thin as possible so as to maximize the relative production in hydrogen, they still induce, on average, more violent reactions, resulting in the production of intermediate-mass fragments with large yields. As a consequence, in the intermediate mass range, the parasite contribution can exceed 50%. This fact, illustrated in Fig. 4, required the same accuracy for the measurement of the parasite reaction as for the production in the full target. In the case of nuclides produced by reactions of charge exchange, the parasite contribution was smaller than 4% for Cs isotopes and smaller than 5% for Ba isotopes.

D. Reconstruction of the angular acceptance

By employing the method exposed so far, we measured for each reaction product the longitudinal-velocity spectrum $dI(v_\parallel^b)/dv_\parallel^b$. This is the distribution of the longitudinal-velocity component $v_\parallel^b$ in the projectile frame corresponding to the portion of the velocity-space distribution $d\sigma/d\boldsymbol{v}^b$ selected by the angular acceptance. The velocity-space distribution could be reconstructed by a deconvolution procedure similar to that introduced in Ref. [18], directly from the measured spectrum $dI(v_\parallel^b)/dv_\parallel^b$. Figure 5 presents in the left column the measured longitudinal-velocity spectra for three intermediate-mass fragments. The corresponding reconstructed velocity-space distributions are shown in the right column by planar cuts along the beam axis. The boundary lines on the planar cuts indicate the angular acceptance of the spectrometer. The cuts on the trajectories along the fragment separator from the target to the exit, defining the angular acceptance, were investigated in Ref. [43]. The probability that a fragment is emitted within these boundaries is defined as the transmission probability f_{tr}, which is equal to unity for the heaviest residues and drops to smaller values for light fragments. This probability is the fraction of reaction products of given mass and atomic number which are selected by the spectrometer.

For light elements up to silicon, the velocity-space distribution was reconstructed as the sum of two components which could be disentangled in the measured longitudinal-velocity spectra, as illustrated in Fig. 5. In general, we observe that the shape of the longitudinal-velocity spectra for the intermediate-mass fragments evolves between two extreme patterns, characterized by a concave and a convex center, respectively. Physically, these two modes reflect the action of the Coulomb field, which acts in different ways depending on the decay process. The velocity-space distribution of the concave mode is an isotropic shell in the frame of the emitting source; this is the effect of the Coulomb repulsion in decay processes with low fragment multiplicity and high fragment-size asymmetry such as, for instance, asymmetric

splits in fission or multifragmentation events characterized by a low multiplicity of fragments. The convex mode can be associated with two very different processes: either residues of sequential evaporation or a much more violent process of multifragmentation in several pieces of comparable size. The asymmetry of the concave component can be fully described as a trivial effect of the angular acceptance (the integral of the forward peak is 14% larger than the integral of the backward peak for ^{11}B and 12% larger than that for ^{31}Si). On the other hand, we attribute the asymmetry of the convex component mainly to the mixing of emission processes associated with different sources: we assume in fact that a large range of excitation energies involved in the formation of a given intermediate-mass fragment would be reflected in a large range in momentum transfer, which is a quantity related to the violence of the reaction [44].

The deconvolution procedure is performed assuming that the velocity-space distribution is composed of several emission processes, which are symmetric with respect to the longitudinal axis; we associate the concave mode to one isotropic source and we describe the asymmetric shape of the convex component by several sources with the same Gaussian shape and different weights. For details see Ref. [45]. The distribution of the emitting sources has to be deduced by an optimization procedure. The hypothesis of isotropic emission from a given source is adapted to relativistic collisions induced by protons. As shown in Fig. 6, the transmission probability obtained by the deconvolution procedure is very different for the two kinematic modes. Also the uncertainties differ remarkably: the large error bars for the convex mode reflect the uncertainty in deducing the distribution of emitting sources and, more generally, the difficulty in determining the width of the distribution of the transverse velocity associated with this mode. In contrast to this, the concave mode is well controlled even at much lower transmission. In Fig. 6, the mass evolution of the transmission probability for intermediate mass fragments is shown: it is the composition of the transmission probability for the concave and convex modes and is labeled as the "multiple-source" approach to indicate that the deconvolution was performed under the assumption that several sources were involved.

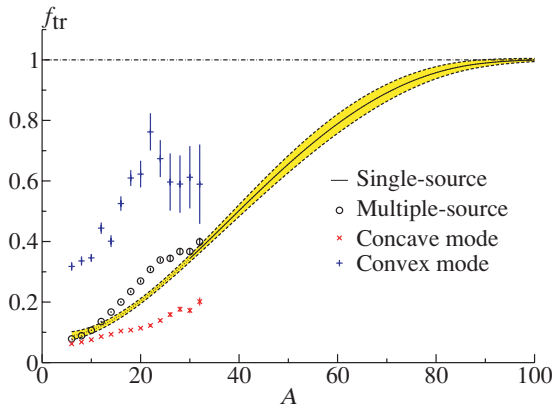

FIG. 6. (Color online) Evolution of the transmission probability f_{tr} as a function of the mass of the fragments, deduced assuming their emission geometry to be either related to one single source or related to more sources. In the latter case, the kinematics is assumed to be the composition of the concave and the convex mode. The transmission evaluated separately for the two kinematic modes is also shown.

For elements above silicon, the two kinematic modes cannot be disentangled any more because the measured integral of the concave mode decreases with respect to the convex mode, and the spacing between the two humps of the concave mode reduces. Besides, the method described so far is necessary if the measured spectra are characterized by a large dispersion of emitting sources, and if, in particular, the convex mode shows a sizable asymmetry and is globally displaced with respect to the concave mode. In this respect, above silicon, this method is much less justified because the whole shape of the measured spectra tends to be symmetric and Gaussian (this trend is visible in Fig. 5). We assumed in this case that all sources contributing to the emission of a given fragment coincide and that the kinematics is fully isotropic. This simplification was applied in the same manner in the analysis of light fragments produced in the spallation of iron [18] where the source velocities of the two kinematic modes contributing to the production of fragments of a given mass were about the same. The mass evolution of the transmission probability calculated with this simple assumption is shown in Fig. 6 and is labeled as the "single-source" approach to indicate that the deconvolution was performed with the assumption that the whole kinematics could reduce to one single source. The smooth function is the result of a fit, and the uncertainty contains the scattering around the function. Such uncertainty reflects the quality of the experimental velocity spectra, which are affected by low statistics in the region of the lowest production yields (around half the mass of the projectile); it reflects also the numerical difficulties in the deconvolution when the transmission probability approaches unity (for $A \approx 80$): in that case, the shape of the angular acceptance affects the results strongly. Above $A \approx 100$, all fragments match the acceptance, and the calculation is trivial. For comparison, the transmission probability for fully isotropic emission is also calculated for the lightest fragments and compared with the multiple-source approach in Fig. 6. The difference between the two approaches is up to 30%.

E. Extraction of primary production cross sections

To extract the production cross section from the production yields, we had to correct for the occurrence of secondary reactions in the layers of matter present along the beam line. Secondary-reaction products formed in the dispersive plane have different consequences on the measurement than those formed in the target area.

A secondary reaction product formed in the dispersive plane deviates from the trajectory related to the magnetic rigidity of the corresponding mother nucleus; it is spatially separated by the ion optics and, with high probability, not transmitted. We corrected for the loss of the primary production by calculating the attenuation of the beam of fragments when traversing the scintillator detector and the degrader. The probability for a nucleus (A_0, Z_0) to traverse a layer of matter of χ atoms per area without interacting is equal to $\mathcal{P}_0 = \exp[-\sigma_0 \chi]$, and

depends on the total reaction cross sections σ_0. The total reaction cross sections were calculated according to the model of Karol [46] modified by Brohm [47], with an uncertainty of 5%. The correction factor for secondary reactions in the dispersive plane f_{DP} is equal to $1/\mathcal{P}_0$; it applies as a multiplicative factor to the measured yields and varies from around 1.05 for the lightest fragments to 1.15 for the heaviest residues; it is illustrated as a function of the mass number of the measured residue in Fig. 7(a).

When secondary reaction products are formed in the target area (liquid hydrogen target), suppressing the secondary fragments by the magnetic spectrometer is not possible because they are produced before entering both dispersive sections. At the same time and with no distinction, we measure a slightly reduced distribution of primary reaction products together with a distribution of secondary reaction products. No direct experimental observables can be related to the loss and gain of production yields due to secondary reactions in the target area. Even though formally we can establish exact relations between the primary and secondary reaction fragments, these relations require the knowledge of the nuclide-production cross sections in the reaction between primary fragments and the target. The correction is therefore dependent on the reaction model we apply.

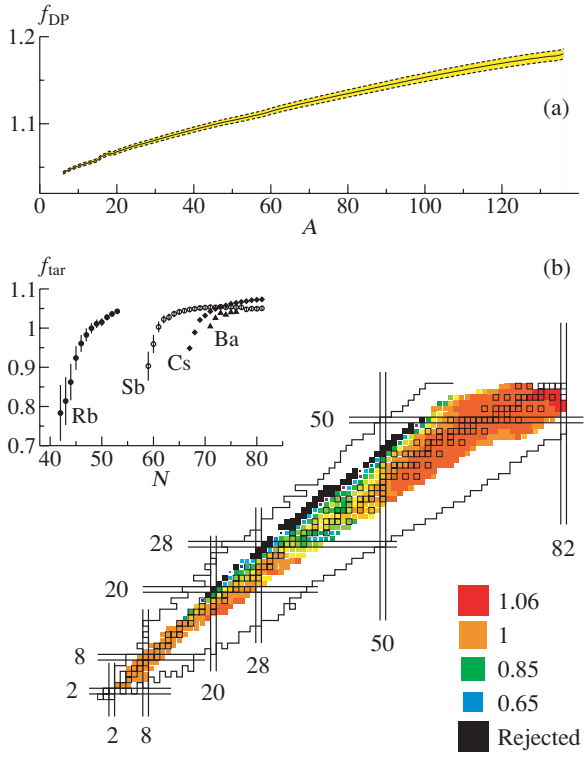

FIG. 7. (Color online) (a) Correction factor for secondary reactions in the dispersive plane f_{DP} (attenuation in the scintillator and the degrader) as a function of the mass number of the residues. The uncertainty is indicated by the colored band. (b) Correction factor for secondary reactions in the target area (liquid hydrogen) f_{tar} on a nuclide chart; in the inset it is illustrated for four elements as a function of the neutron number.

The nuclide-production cross sections in the secondary reactions were calculated by coupling the models BURST [48] and ABLA [48–50]; the former is a parametrization of the intranuclear cascade, the latter models the decay of hot fragments. To calculate the correction factor, we used the same method of Ref. [51] employed in the analysis of a recent experiment on the spallation of ^{238}U [12]. The method evaluates the secondary production yields in a thick target in inverse kinematics at relativistic energies. In the analysis of the spallation of ^{238}U, the method considered decays by evaporation and fission; in the present analysis, we employed this method in a reduced form, excluding fission, even though we expect its contributions in the production of intermediate-mass fragments in the spallation of xenon. The modeling of these particular channels is not well controlled at this incident energy due to a lack of experimental data. For this reason, the correction factor was set equal to unity for light fragments. Since heavy fragments are mostly produced by evaporation, their correction factor is not much affected by this limitation. The result of the calculation is shown in Fig. 7(b) on a nuclide chart. The correction factor for secondary reactions in the target f_{tar} (multiplicative coefficient applied to the measured production yields) is set to unity for the lightest fragments up to aluminum. It then decreases gradually from unity down to about 0.8 for the isotopes of nickel; it increases monotonically for heavier elements, and in the region of zirconium it exceeds unity, up to the largest value 1.06 attained in proximity of ^{136}Xe.

The global effect of the secondary reactions in the target is to reduce the yields of the heaviest elements in favor of those fragments having around half the mass of the projectile, which are also the least produced. Moreover, evaporation residues are mostly produced in the neutron-deficient side of the chart of the nuclides, with the consequence that secondary reactions have the effect of decreasing the yields of neutron-rich fragments in favor of less neutron-rich fragments. This tendency is illustrated in Fig. 7(b) and in the corresponding inset, where the evolution of the correction factor is studied for four elements as a function of the neutron number. In the case of Cs and Ba, the loss of cross section due to secondary spallation reactions producing lighter residues is compensated by the gain of cross section due to secondary reactions of charge exchange. The uncertainty in the correction factor depends on two quantities. First, it depends on the uncertainty of the calculation of the total reaction cross sections which, also in this case, were obtained from the model of Karol [46] modified by Brohm [47], with an uncertainty of 5%. Second, it depends on the uncertainty that we attribute to the model calculation of the nuclide-production cross sections in the secondary reactions: according to the simulation of measured spallation data (see, e.g., Ref. [14]), we estimated that this uncertainty is as large as 20%. This second contribution most strongly affects the nuclides which are largely produced by secondary reactions, and the uncertainty is larger for nuclides associated with smaller correction factors, as illustrated in the inset of Fig. 7(b).

The experimental method turns out to be limited for the measurement of neutron-deficient residues as their yields are completely dominated by secondary reactions. Yields fed by secondary reactions for more than 50% were rejected.

IV. EXPERIMENTAL RESULTS

The average kinetic energies were deduced from the reconstructed velocity-space distributions $d\sigma/d\boldsymbol{v}^b$. From the same unfolding procedure, as discussed in Sec. III E, the nuclide cross sections were obtained from integrating the reconstructed velocity spectra and correcting for secondary reactions, so that the production cross sections were deduced as

$$\sigma = I f_{\rm tr} f_{\rm tar} f_{\rm DP}, \tag{9}$$

where $f_{\rm tr}$ is the transmission probability, $f_{\rm tar}$ the correction for secondary reactions in the target, and $f_{\rm DP}$ the correction for secondary reactions in the dispersive plane.

A. Kinetic energies

A general survey of the average kinetic energy imparted to the spallation residues is presented as a function of the mass number in Fig. 8, and the data are listed in Table II. It results from the decay kinematics as well as from the displacement of the emitting source in the beam frame as a consequence of the collision. The latter contribution is shown in a separate spectrum in Fig. 8. The average kinetic energies were deduced from the velocity-space distribution reconstructed according to the multiple-source prescription described in Sec. III D up to $A = 30$. The error bars reflect the uncertainty in the fit of the measured longitudinal-velocity distribution, the uncertainty in the unfolding procedure, and the statistics of the measurement. The enlarging of the error bars in approaching $A = 30$ reflects the increasing difficulty in applying the multiple-source prescription to the measured longitudinal-velocity distribution which, becoming gradually closer to a Gaussian distribution, progressively reduces the information for estimating the asymmetry of the emission kinematics. For masses larger than $A = 30$ we switched to the single-source prescription, because the measured velocity spectra are, in general, Gaussian-like. The mismatch at $A = 30$

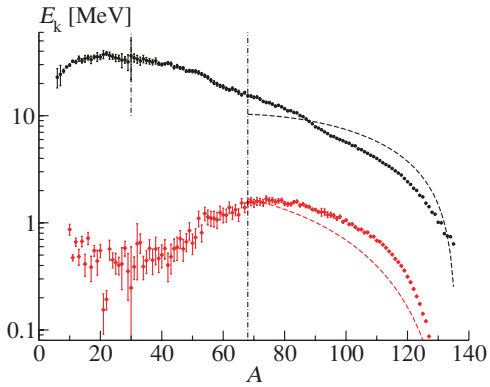

FIG. 8. (Color online) Distribution of mean kinetic energies in the projectile frame averaged over isobaric chains is represented by the upper spectrum. The lower spectrum indicates the contribution to the mean kinetic energy that is attributed to the mean momentum transfer during the impact. The difference between the two spectra is the kinetic energy gained in the decay. The error bars include both statistical and systematical errors. A vertical line separates the portion of the upper spectrum related to fragments lighter than $A = 30$, evaluated according to the multiple-source prescription, from the rest of the spectrum, evaluated according to the single-source prescription. The diagram is divided in two parts corresponding to half the mass of the projectile. In the heavier mass portion, both experimental spectra are compared with the Morrissey systematics [44] (dashed line).

TABLE II. Kinetic energies in the projectile frame averaged over isobaric chains. The uncertainty, indicated in parenthesis, includes both statistical and systematical errors and applies to the last decimal digits.

A	E_k (MeV)	A	E_k (MeV)	A	E_k (MeV)
6	22.87 ± 4.72	50	26.07(94)	94	6.824(67)
7	24.30 ± 5.24	51	25.94(95)	95	6.476(61)
8	26.17 ± 1.11	52	25.35(92)	96	6.384(61)
9	28.50(42)	53	24.48(81)	97	6.146(59)
10	29.73(78)	54	23.60(86)	98	5.994(51)
11	32.17(77)	55	22.81(85)	99	5.844(61)
12	31.81 ± 1.18	56	21.43(80)	100	5.651(59)
13	34.12 ± 1.97	57	20.37(81)	101	5.531(51)
14	32.52 ± 1.53	58	19.71(77)	102	5.270(52)
15	34.06 ± 2.49	59	18.98(69)	103	5.221(52)
16	34.95 ± 1.86	60	18.64(81)	104	4.903(47)
17	33.37 ± 2.73	61	17.88(64)	105	4.815(46)
18	35.39 ± 1.46	62	17.43(56)	106	4.614(43)
19	35.50 ± 3.32	63	17.92(65)	107	4.462(40)
20	35.30 ± 1.89	64	17.27(57)	108	4.285(39)
21	37.26 ± 3.21	65	16.55(76)	109	4.157(36)
22	38.13 ± 1.70	66	15.73(45)	110	3.991(39)
23	36.51 ± 2.80	67	16.42(49)	111	3.812(35)
24	35.62 ± 2.05	68	15.33(40)	112	3.638(27)
25	34.67 ± 2.66	69	15.24(43)	113	3.499(31)
26	34.42 ± 2.35	70	14.83(40)	114	3.374(28)
27	32.99 ± 4.93	71	14.91(41)	115	3.220(28)
28	33.26 ± 2.34	72	14.31(37)	116	3.058(26)
29	31.76 ± 5.34	73	13.60(30)	117	2.915(24)
30	36.2 ± 14.6	74	13.30(32)	118	2.796(23)
31	34.72 ± 3.08	75	13.23(28)	119	2.592(18)
32	33.83 ± 2.89	76	12.85(27)	120	2.419(20)
33	32.49 ± 2.85	77	12.29(24)	121	2.284(18)
34	33.92 ± 2.74	78	12.49(24)	122	2.104(16)
35	32.82 ± 2.21	79	12.12(22)	123	2.006(15)
36	32.31 ± 2.01	80	11.62(20)	124	1.808(14)
37	31.59 ± 1.87	81	11.11(19)	125	1.749(13)
38	32.50 ± 2.18	82	11.14(15)	126	1.526(11)
39	30.65 ± 1.10	83	10.74(13)	127	1.4158(95)
40	30.06(93)	84	10.62(12)	128	1.2543(78)
41	30.51(76)	85	10.06(12)	129	1.2044(75)
42	31.06 ± 1.06	86	9.80(11)	130	1.0130(54)
43	30.43 ± 1.31	87	9.328(97)	131	1.0008(58)
44	28.31 ± 1.04	88	8.852(86)	132	0.7930(30)
45	29.01 ± 1.11	89	8.406(79)	133	0.7536(37)
46	27.97(78)	90	7.878(71)	134	0.7429(10)
47	27.73(99)	91	7.674(72)	135	0.63480(82)
48	26.07(72)	92	7.393(81)		
49	26.30(84)	93	7.071(79)		

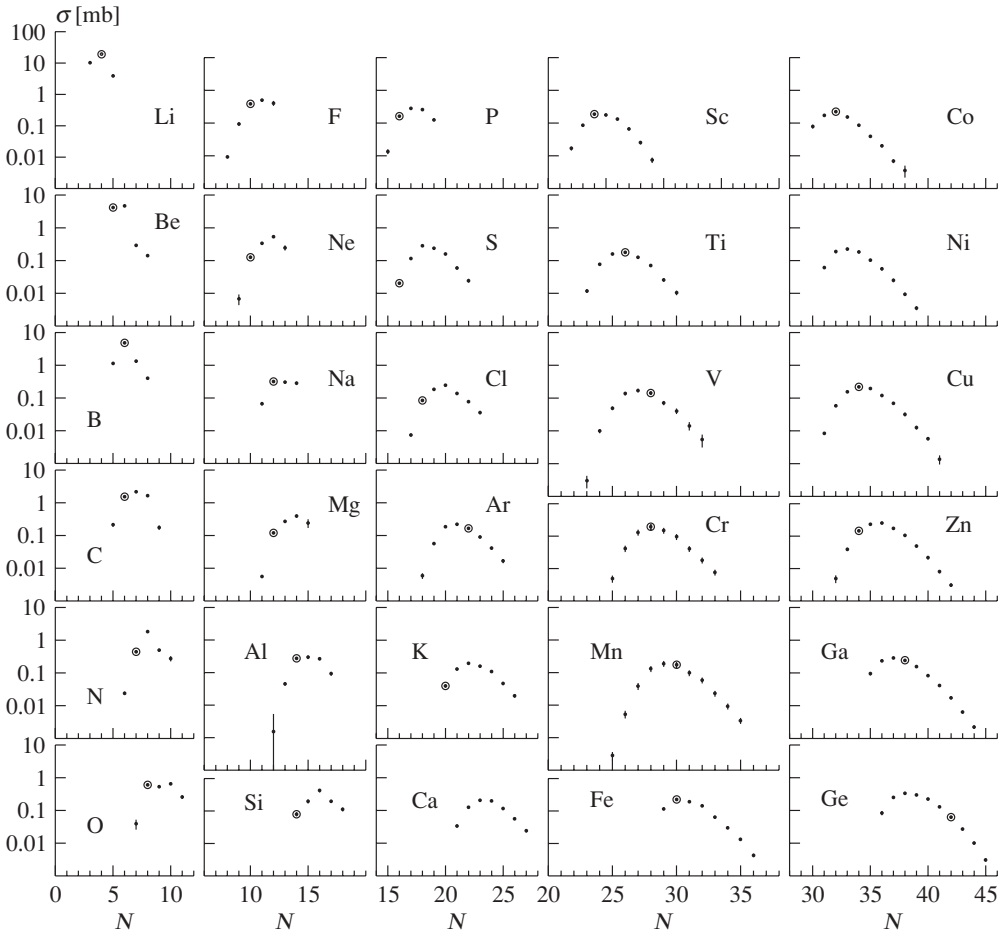

FIG. 9. Production cross sections for the isotopes of elements ranging from Li to Ge. Circles indicate the stable isotopes with the highest natural abundance.

indicates that the kinematics is still not isotropic in this mass range, and the two approaches are not yet equivalent.

For the heaviest fragments, which are characterized by measured longitudinal velocity spectra with Gaussian shape, of width σ_v and mean value $\langle v_\parallel^b \rangle$, the kinetic energy is given by $E_k = (1/2)m_0 A(\langle v_\parallel^b \rangle^2 + 3\sigma_v^2)$. The heaviest fragments are qualitatively consistent with the systematics of Morrissey [44], which was deduced from residues of sequential evaporation in very peripheral ion-ion collisions. This systematics correlates the mean value and the width of the momentum-transfer distribution in the projectile frame to the mass loss and to the square root of the mass loss, respectively.

B. Production cross sections

The experimental production cross sections are collected in Tables III and IV and shown as isotopic distributions in Figs. 9 and 10. Despite an effort to measure the cross sections down to the μb level, the measurement of very low cross sections was, for neutron-deficient nuclides, hindered by large feeding from secondary reactions in the target. The total uncertainty rarely exceeds 15% for the lightest nuclides and is below 10% on average for the heavy nuclides. There are two main contributions to the uncertainties. The first concerns mostly the intermediate-mass fragments: the procedures of analysis, fitting of the velocity spectra and velocity reconstruction, being strongly constrained by the knowledge of the ion optics of the spectrometer, depend strongly on the resolution of the spectra and, therefore, depend first on the acquisition statistics; this contribution is reflected in the uncertainty of the transmission probability (see Fig. 6). The second contribution is systematical: the uncertainty in the calibration of the beam monitor is constant for the whole ensemble of nuclide cross sections (5%); the correction for the secondary reactions in the beam line introduces uncertainties which depend on the total reaction cross sections calculated for the secondary interactions [see Fig. 7(a)]; the correction for the secondary reactions in the target introduces uncertainties which vary strongly as a function of the nuclide and penalize the less neutron-rich fragments [see Fig. 7(b)]. The formation cross sections were deduced for each measured nuclide, for the intermediate-mass fragments, for the heavy residues, and even for the production of two elements, cesium and barium, by charge exchange.

Integrating all measured production cross sections, a value of 1393 ± 72 mb was obtained. Deducing the total reaction

TABLE III. Isotopic cross sections for the production of elements ranging from Li to Tc. The uncertainty includes statistical and systematical errors. Where indicated in parenthesis, it applies to the last decimal digits.

A	σ (mb)	A	σ (mb)	A	σ (mb)	A	σ (mb)	A	σ (mb)	A	σ (mb)	A	σ (mb)
	Li	26	0.0453(56)	47	0.0241(28)	59	0.0648(56)	74	0.00639(61)	80	0.605(43)	92	0.675(36)
6	10.12(59)	27	0.271(29)		Sc	60	0.0306(29)	75	0.00223(28)	81	0.501(31)	93	0.383(20)
7	19.0 ± 1.1	28	0.294(34)	43	0.0168(23)	61	0.0134(15)		Ge	82	0.358(21)	94	0.195(10)
8	3.90(30)	29	0.268(31)	44	0.0862(67)	62	0.00433(52)	68	0.084(12)	83	0.212(12)	95	0.0885(47)
	Be	30	0.092(13)	45	0.188(13)		Co	69	0.251(20)	84	0.1036(61)	96	0.0383(21)
9	4.20(25)		Si	46	0.177(13)	57	0.079(10)	70	0.334(24)	85	0.0413(25)	97	0.01513(91)
10	4.61(28)	28	0.080(11)	47	0.1323(99)	58	0.174(14)	71	0.295(20)	86	0.01469(96)	98	0.00549(47)
11	0.290(23)	29	0.199(27)	48	0.0665(58)	59	0.220(17)	72	0.223(15)	87	0.00536(41)	99	0.00114(27)
12	0.142(10)	30	0.427(53)	49	0.0251(30)	60	0.155(12)	73	0.1293(91)	88	0.00158(36)		Nb
	B	31	0.199(22)	50	0.0074(14)	61	0.0863(72)	74	0.0619(47)		Rb	87	0.045(14)
10	1.131(73)	32	0.113(16)		Ti	62	0.0390(36)	75	0.0272(21)	79	0.158(15)	88	0.324(39)
11	4.88(29)		P	45	0.0118(16)	63	0.0200(19)	76	0.01013(87)	80	0.398(33)	89	1.067(87)
12	1.33(10)	30	0.0135(22)	46	0.0778(62)	64	0.00687(90)	77	0.00309(37)	81	0.690(50)	90	2.28(13)
13	0.406(27)	31	0.164(11)	47	0.159(12)	65	0.0036(14)		As	82	0.778(49)	91	2.70(15)
	C	32	0.278(18)	48	0.177(13)		Ni	70	0.0713(88)	83	0.747(44)	92	1.813(96)
11	0.212(28)	33	0.259(17)	49	0.1263(95)	59	0.0619(44)	71	0.220(18)	84	0.530(30)	93	1.440(75)
12	1.528(92)	34	0.1253(97)	50	0.0699(59)	60	0.187(20)	72	0.347(24)	85	0.348(20)	94	0.984(51)
13	2.15(13)		S	51	0.0254(29)	61	0.226(20)	73	0.374(25)	86	0.1747(99)	95	0.647(34)
14	1.65(12)	32	0.0201(17)	52	0.0104(16)	62	0.182(16)	74	0.270(18)	87	0.0708(41)	96	0.351(18)
15	0.176(27)	33	0.1155(75)		V	63	0.103(10)	75	0.199(13)	88	0.0272(16)	97	0.1731(90)
	N	34	0.285(18)	46	0.00030(12)	64	0.0561(66)	76	0.1025(67)	89	0.01024(68)	98	0.0792(42)
13	0.0241(28)	35	0.240(16)	47	0.0099(14)	65	0.0250(31)	77	0.0500(34)	90	0.00361(31)	99	0.0338(19)
14	0.446(33)	36	0.159(12)	48	0.0492(63)	66	0.0094(11)	78	0.0198(14)		Sr	100	0.01338(82)
15	1.85(13)	37	0.0591(56)	49	0.137(17)	67	0.00352(48)	79	0.00706(60)	81	0.084(22)		Mo
16	0.499(38)	38	0.0244(32)	50	0.172(20)		Cu	80	0.00291(44)	82	0.360(46)	90	0.269(47)
17	0.276(50)		Cl	51	0.141(18)	60	0.00845(71)	81	0.00104(52)	83	0.795(59)	91	1.205(96)
	O	34	0.00737(61)	52	0.071(11)	61	0.0585(43)		Se	84	1.058(67)	92	2.54(16)
15	0.039(13)	35	0.0854(57)	53	0.0403(78)	62	0.157(11)	72	0.0653(97)	85	1.049(60)	93	3.16(17)
16	0.603(40)	36	0.184(12)	54	0.0143(41)	63	0.221(16)	73	0.229(18)	86	0.822(46)	94	2.62(14)
17	0.534(38)	37	0.245(16)	55	0.0054(23)	64	0.194(14)	74	0.422(30)	87	0.526(29)	95	2.05(11)
18	0.656(50)	38	0.139(10)		Cr	65	0.1203(98)	75	0.407(31)	88	0.277(15)	96	1.299(67)
19	0.256(33)	39	0.0774(68)	49	0.0049(12)	66	0.0689(66)	76	0.322(28)	89	0.1283(71)	97	0.912(47)
	F	40	0.0358(40)	50	0.0415(92)	67	0.0321(41)	77	0.208(19)	90	0.0512(29)	98	0.574(30)
17	0.00925(79)		Ar	51	0.131(27)	68	0.0126(16)	78	0.150(10)	91	0.0202(12)	99	0.303(16)
18	0.095(10)	36	0.0059(11)	52	0.196(40)	69	0.00572(62)	79	0.0820(51)	92	0.00792(55)	100	0.1451(75)
19	0.388(28)	37	0.0564(44)	53	0.149(31)	70	0.00136(42)	80	0.0362(23)	93	0.00270(34)	101	0.0678(36)
20	0.494(44)	38	0.185(12)	54	0.096(20)		Zn	81	0.01303(92)		Y	102	0.0306(17)
21	0.404(70)	39	0.218(15)	55	0.0410(84)	62	0.0049(13)	82	0.00449(39)	84	0.307(41)	103	0.01050(73)
	Ne	40	0.165(12)	56	0.0181(37)	63	0.0393(46)	83	0.00098(19)	85	0.800(65)	104	0.00378(52)
19	0.0068(24)	41	0.0910(73)	57	0.0077(16)	64	0.145(11)		Br	86	1.298(80)		Tc
20	0.126(13)	42	0.0415(43)		Mn	65	0.233(17)	74	0.0377(87)	87	1.436(82)	92	0.301(37)
21	0.336(28)	43	0.0167(24)	50	0.000280(81)	66	0.254(18)	75	0.216(17)	88	1.197(65)	93	1.23(10)
22	0.538(44)		K	51	0.0053(14)	67	0.173(13)	76	0.428(29)	89	0.796(43)	94	2.87(16)
23	0.247(45)	39	0.0399(36)	52	0.0384(93)	68	0.1044(85)	77	0.510(37)	90	0.440(24)	95	3.79(20)
	Na	40	0.1328(92)	53	0.131(27)	69	0.0495(50)	78	0.387(34)	91	0.218(12)	96	3.51(19)
22	0.0677(80)	41	0.198(14)	54	0.189(39)	70	0.0216(26)	79	0.347(25)	92	0.0978(53)	97	3.19(17)
23	0.321(22)	42	0.162(12)	55	0.174(36)	71	0.00798(88)	80	0.223(14)	93	0.0446(25)	98	2.44(13)
24	0.305(21)	43	0.1108(86)	56	0.098(20)	72	0.00311(38)	81	0.1365(83)	94	0.01625(97)	99	1.772(94)
25	0.282(35)	44	0.0473(47)	57	0.058(12)		Ga	82	0.0583(36)	95	0.00596(44)	100	1.115(61)
	Mg	45	0.0201(27)	58	0.0227(47)	66	0.096(12)	83	0.0244(16)	96	0.00228(28)	101	0.677(38)
23	0.00559(46)		Ca	59	0.0092(19)	67	0.238(18)	84	0.00833(60)		Zr	102	0.351(21)
24	0.1196(91)	41	0.0336(31)	60	0.00333(69)	68	0.288(20)	85	0.00221(23)	86	0.188(46)	103	0.165(11)
25	0.271(27)	42	0.1245(89)		Fe	69	0.245(17)		Kr	87	1.060(81)	104	0.0705(58)
26	0.394(44)	43	0.204(14)	55	0.116(10)	70	0.156(11)	76	0.0343(90)	88	1.51(10)	105	0.0287(33)
27	0.242(72)	44	0.196(14)	56	0.226(17)	71	0.0830(69)	77	0.204(16)	89	1.87(11)	106	0.0101(23)
	Al	45	0.1149(87)	57	0.193(15)	72	0.0413(36)	78	0.484(33)	90	1.587(86)		
25	0.0015(38)	46	0.0560(51)	58	0.144(11)	73	0.0173(15)	79	0.574(44)	91	1.069(56)		

TABLE IV. Isotopic cross sections for the production of elements ranging from Ru to Ba. The uncertainty includes both statistical and systematical errors. Where indicated in parenthesis, it applies to the last decimal digits. Underlined values are deduced from systematics.

A	σ (mb)	A	σ (mb)	A	σ (mb)	A	σ (mb)	A	σ (mb)	A	σ (mb)
	Ru	110	0.698(38)	118	0.281(16)	119	5.85(30)	118	9.88(50)	118	0.121(18)
95	1.174(85)	111	0.348(20)	119	0.1341(90)	120	4.15(21)	119	11.68(59)	119	0.395(23)
96	2.99(17)	112	0.163(11)	120	0.0660(60)	121	2.79(14)	120	13.44(68)	120	0.954(52)
97	4.42(23)	113	0.0744(59)	121	0.0288(46)	122	1.914(99)	121	14.39(73)	121	1.594(85)
98	4.66(24)	114	0.0317(33)	122	0.0121(12)	123	1.232(64)	122	14.09(71)	122	2.86(15)
99	4.29(22)	115	0.0140(84)	123	0.0050(10)	124	0.717(39)	123	13.88(70)	123	3.92(20)
100	3.85(20)		Ac	124	0.00194(37)	125	0.418(24)	124	12.44(63)	124	5.76(30)
101	2.86(15)	101	0.480(53)	125	0.000690(61)	126	0.227(12)	125	11.00(56)	125	6.98(36)
102	1.92(10)	102	1.95(12)		In	127	0.106(11)	126	9.44(48)	126	9.10(46)
103	1.142(62)	103	4.77(25)	105	0.092(24)	128	0.0517(59)	127	8.42(43)	127	10.27(52)
104	0.632(36)	104	7.21(37)	106	0.760(59)	129	0.0198(11)	128	6.68(34)	128	12.71(64)
105	0.321(19)	105	8.19(42)	107	2.72(15)	130	0.00560(33)	129	5.26(27)	129	13.63(69)
106	0.157(11)	106	8.56(44)	108	5.81(31)		Sb	130	4.26(22)	130	15.79(80)
107	0.0581(53)	107	8.14(42)	109	8.49(44)	110	0.1330(87)	131	3.41(17)	131	17.34(88)
108	0.0246(59)	108	6.80(35)	110	9.87(51)	111	0.664(38)	132	2.87(15)	132	21.2 ± 1.1
109	0.0053(23)	109	5.40(28)	111	11.37(58)	112	2.23(12)	133	1.249(65)	133	23.3 ± 1.2
	Rh	110	3.72(19)	112	11.00(56)	113	4.85(25)	134	0.305(15)	134	31.5 ± 1.6
97	0.961(85)	111	2.49(13)	113	10.14(52)	114	6.85(35)		I	135	54.7 ± 2.8
98	2.69(16)	112	1.428(76)	114	8.43(43)	115	10.01(51)	113	0.00122(17)		Cs
99	4.91(26)	113	0.844(46)	115	6.46(33)	116	11.86(60)	114	0.0107(10)	122	0.145(11)
100	5.63(29)	114	0.405(23)	116	4.79(25)	117	13.33(68)	115	0.0798(53)	123	0.275(18)
101	5.75(30)	115	0.232(14)	117	3.24(17)	118	13.29(68)	116	0.448(26)	124	0.536(32)
102	5.19(27)	116	0.1067(79)	118	2.05(11)	119	12.80(65)	117	1.247(67)	125	0.773(43)
103	4.30(22)	117	0.0468(43)	119	1.331(70)	120	11.21(57)	118	2.31(12)	126	1.153(63)
104	3.08(16)	118	0.0197(35)	120	0.755(40)	121	9.92(50)	119	4.09(21)	127	1.525(81)
105	2.07(11)	119	0.0087(17)	121	0.438(24)	122	7.82(40)	120	6.00(31)	128	1.95(10)
106	1.230(66)	120	0.00348(74)	122	0.249(15)	123	6.07(31)	121	8.48(43)	129	2.28(12)
107	0.702(39)	121	0.001550(93)	123	0.1320(82)	124	4.76(24)	122	10.11(51)	130	2.81(15)
108	0.336(20)	122	0.000420(37)	124	0.0580(61)	125	3.46(18)	123	12.76(65)	131	2.97(15)
109	0.163(11)		Cd	125	0.0290(41)	126	2.41(12)	124	13.24(67)	132	3.12(16)
110	0.0674(54)	104	1.26(11)	126	0.0128(15)	127	1.677(87)	125	15.39(78)	133	2.94(15)
111	0.0256(41)	105	3.80(22)	127	0.00420(23)	128	1.040(56)	126	14.97(76)	134	2.65(14)
	Pd	106	7.06(37)		Sn	129	0.542(29)	127	16.51(84)	135	1.415(73)
99	0.722(70)	107	8.49(44)	108	0.358(31)	130	0.290(15)	128	14.85(75)	136	0.499(28)
100	2.49(15)	108	9.73(50)	109	1.628(94)	131	0.1414(75)	129	17.12(87)		Ba
101	4.94(26)	109	10.03(51)	110	4.34(23)	132	0.0396(20)	130	14.66(74)	127	0.0242(37)
102	6.85(35)	110	9.04(46)	111	7.38(38)		Te	131	16.38(83)	128	0.0326(47)
103	6.91(36)	111	7.55(39)	112	9.48(49)	111	0.00777(63)	132	14.53(73)	129	0.0381(45)
104	7.07(36)	112	5.79(30)	113	11.77(60)	112	0.0565(35)	133	15.40(78)	130	0.0267(39)
105	6.11(31)	113	4.08(21)	114	12.49(64)	113	0.289(16)	134	21.9 ± 1.1	131	0.0228(36)
106	4.79(25)	114	2.70(14)	115	12.43(63)	114	1.152(61)	135	23.6 ± 1.2	132	0.0147(29)
107	3.35(17)	115	1.645(86)	116	11.45(58)	115	2.97(15)		Xe		
108	2.22(12)	116	0.929(50)	117	9.58(49)	116	4.76(25)	116	0.00258(35)		
109	1.322(71)	117	0.547(30)	118	7.80(40)	117	7.37(38)	117	0.0188(19)		

cross section is not straightforward, because the multiplicity of products from binary decays and multifragmentation is larger than unity. These decay channels are, however, expected to contribute to a small fraction of the total reaction cross section (around 5%, according to Ref. [45]). In addition, products with $Z < 3$ are not measured. When we assume that products with $Z < 3$ are always accompanied by heavier fragments, the sum of the measured production cross section is an upper estimate of the total interaction cross section. The geometric cross section calculated by the model of Karol [46] modified by Brohm [47], which is 1353 mb, is consistent with our result.

A detailed survey of the distribution of nuclide cross sections reveals the presence of staggering effects. In the region of the light nuclides, these are visible in the distribution of production cross sections for specific values of $N - Z$, as shown in Fig. 11(a); the staggering is also visible in the isotopic distribution of the heaviest residues such as xenon and iodine, as shown in Fig. 11(c).

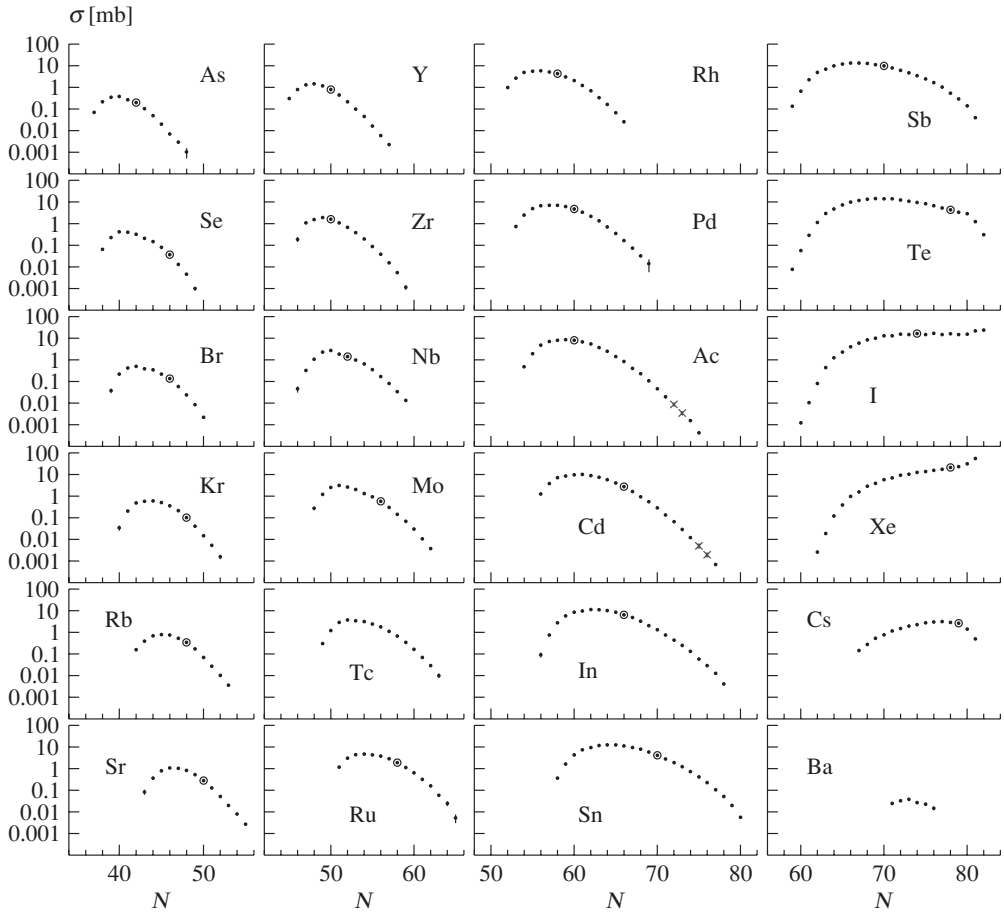

FIG. 10. Production cross sections for the isotopes of elements ranging from As to Ba. Cross sections indicated by crosses were deduced from systematics. Circles indicate the stable isotopes with the highest natural abundance.

The production cross sections are summarized on the nuclide chart and represented with projections along the element and neutron number in Fig. 12. The general feature is the U shape of the element- and neutron-number distributions, which range over about two orders of magnitude.

V. DISCUSSION

Without entering into the discussion on the phenomenology of the reaction, which is beyond the purpose of this report, we conclude by pointing out some physics cases which will be the subject of further research; they are related, on the one hand, to the fine structure in the nuclide cross section and, on the other hand, to the gross properties of the nuclide production.

A. Fine structure in the nuclide cross sections

The cross section fluctuates between neighboring nuclides signing the presence of strong fine-structure effects. As shown in Fig. 11(a), the fine structure manifests over chains on nuclides with the same value of $N - Z$. An "even-odd" staggering characterizes chains of nuclides having $N - Z \leqslant 0$. For $N - Z > 0$, the staggering is even-odd, with a higher production of even nuclides, for all chains of even value of $N - Z$, but it reverses, with a higher production of odd nuclides, for odd values of $N - Z$ for neutron-rich nuclides. The amplitude of the staggering can be quantified with the procedure introduced by Tracy [52], like in the analysis of the residue production from fragmentation reactions in Ref. [53]. The result of the Tracy analysis applied to the cross sections of Fig. 11(a) is shown in Fig. 11(b). The highest amplitude of the even-odd staggering is measured for the chain $N - Z = 0$, and it may exceed 40%. A lower but still large amplitude of the even-odd staggering characterizes the other even value of $N - Z$: it evolves from 30% to 10% for the chain $N - Z = 2$, below chlorine. A similar evolution of the amplitude can be appreciated for the inverse even-odd staggering, which characterizes the chains with odd values of $N - Z > 0$, such as $N - Z = 3$. In the regions of the chart of nuclides where the neutron-rich side is more populated than the neutron-deficient side, if fine-structure effects are present, they amplify in an even-odd staggering when the nuclide cross sections are projected on the neutron-number axis, and they compensate, resulting in a smoothed staggering, when projected on the atomic-number axis. The atomic- and neutron-number projections shown in Fig. 12 manifest this phenomenology: the strong even-odd staggering characterizing the neutron-number

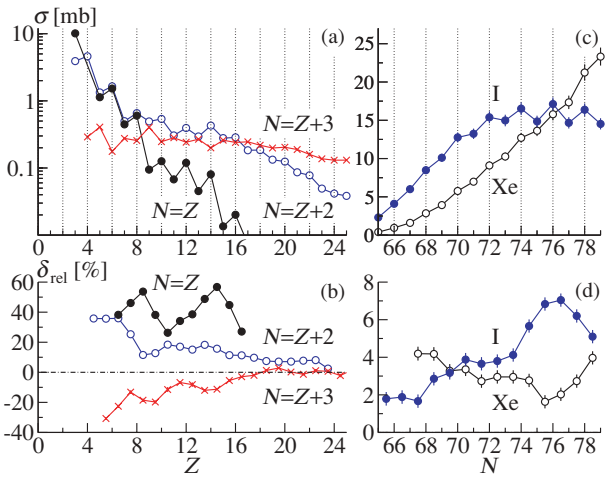

FIG. 11. (Color online) (a) An even-odd staggering in the production cross section of the residues manifests for chains of even value of $N - Z$ with a higher production of even nuclides, and it reverses, with a higher production of odd nuclides, for odd values of $N - Z$ for neutron-rich nuclides. (b) Staggering amplitude of the cross sections shown in (a) analyzed by the method of Tracy [52]. It is positive when the staggering is even-odd and negative when the staggering reverses. (c) Even-odd staggering in the production cross sections of the isotopes of xenon and iodine in $^{136}\mathrm{Xe}_{(1A\,\mathrm{GeV})}+p$. (d) Staggering amplitude of the cross sections shown in (c) analyzed by the method of Tracy [52].

distribution appears in correspondence with portions of the chart of nuclides where neutron-rich sides are most populated; these are two regions: the intermediate-mass fragments and the very heavy nuclides. These regions can be easily identified in Fig. 13, where the average neutron-to-proton ratio $\langle N/Z\rangle$ of the nuclides is shown.

The staggering is understandable in relation to the decay process. Concerning the region of intermediate-mass fragments, previous measurements of highly excited systems [53,54] already revealed the same kind of staggering. It was suggested that the effect should be related to the reconstitution of fine-structure effects in the level densities during the cooling of the nucleus. In particular, the formation of the intermediate-mass fragments is consistent with a process ending with at least a few evaporation steps which are responsible for the appearing of the staggering. Concerning the heaviest elements, mostly xenon and iodine, we observe an even-odd staggering along the isotopic distribution with an amplitude approaching a value of 8% in the case of iodine, as shown in Figs. 11(c) and 11(d). This feature is consistent with the appearance of strong pairing correlations due to the low angular momentum which characterizes the production of the heaviest fragments [55,56].

B. Gross features on the nuclide production of nuclides

As a general feature, the production cross section can be divided in three portions: a large production of intermediate-mass fragments, a deep hollow in the region around about half the mass of the projectile, and a large production of heavy

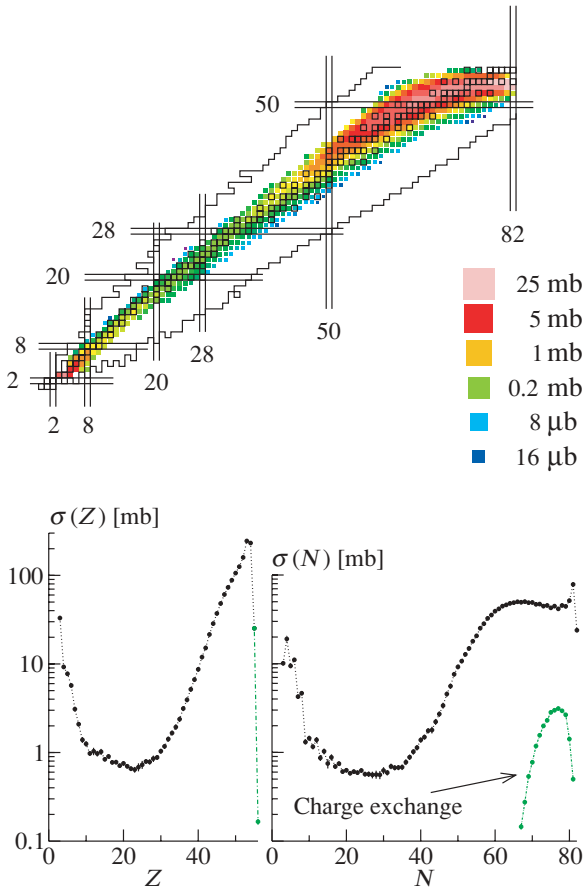

FIG. 12. (Color online) Nuclide production cross sections represented on the nuclide chart. Colors vary according to a logarithmic scale. The lower panel presents the projections of the residue-production cross sections along the atomic and neutron number. The charge-exchange contribution is also indicated in the projections.

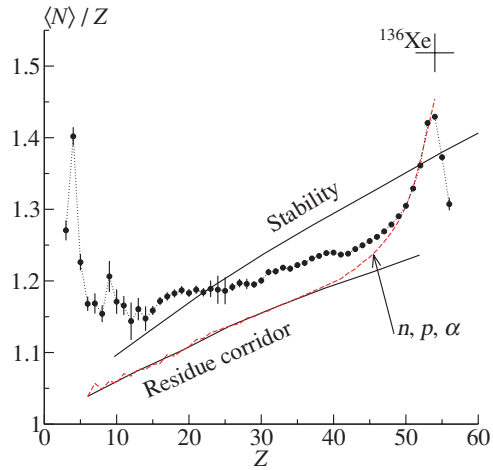

FIG. 13. (Color online) Evolution of the quantity $\langle N/Z\rangle$ as a function of the element number. The dashed line is a calculation in which evaporation was limited to the emission of neutrons, protons, and α particles.

residues. Such a distribution has always been observed for the decay of highly excited systems [31].

The kinetic energies of the fragments give hints of the reaction kinematics. As shown in Fig. 8, the part of the experimental spectrum related to the intermediate-mass-fragment production deviates in favor of very high kinetic energies from the systematics, which describes the contribution from the heaviest residue of one decay sequence, characterized by a larger number of small recoils from evaporation of particles and light fragments. In the part of the spectrum where the mass of the residues is lower than half the mass of the projectile, the deviation from the systematics is due to the predominant contribution of the light partner of a binary decay or a product of a multifragmentation event characterized by a high kinetic energy. As shown in Fig. 13, the average neutron-to-proton ratio $\langle N/Z \rangle$ of the nuclides indicates that the intermediate-mass fragments are neutron rich, and they gradually migrate toward the stability valley, which is attained in the region of the hollow, around titanium. In addition to the high kinetic energies, the extension of the production to neutron-rich nuclides and the U shape of the production are properties of fission below the Businaro-Gallone point as well as multifragmentation of a neutron-rich source [57].

The heavy spallation residues, close to the mass of the projectile, constitute the largest fraction of the reaction cross section and correspond to the evaporation of mostly nucleons and clusters. More in detail, as shown in Fig. 14, the evolution of the cross section of the heavy residues as a function of the mass loss presents initially a steep fall for the loss of the first few mass units, followed by a plateau up to a mass loss of about 20 units, which changes gradually into an almost exponential descent beyond around $\Delta A = 40$. The plateau, which is most evident as a function of the neutron number, as shown in Fig. 12 for the system ^{136}Xe+p, corresponds to a large loss of neutrons. In fact, quite independently of the neutron enrichment of the hot spallation residues, the sequential evaporation process is expected to direct the decay toward the residue corridor [58]; in the region of heavy nuclides, this is located in the neutron-deficient side of the nuclide chart and corresponds to the situation which could be described as [59] $dN/dZ = \langle \Gamma_N / \Gamma_Z \rangle$, where Γ_Z and Γ_N are the proton and neutron emission widths, respectively. The plateau corresponds therefore to the rapid migration of the average neutron-to-proton ratio $\langle N/Z \rangle$, which indicates the ridge of the production of residues, toward the residue corridor, as shown in Fig. 13. For elements ranging down to tin, the evolution of $\langle N/Z \rangle$ is compatible with a calculation in which only neutrons, protons, and α particles are emitted (dashed line in Fig. 13). Below tin, this simplified evaporation pattern would evolve for light elements toward the residue corridor. On the contrary, the residue corridor is never reached; the ridge of the measured production moves gradually away from the neutron-deficient side of the nuclide chart, to finally join the neutron-rich side of the nuclide chart, which is populated by the intermediate-mass fragments. Correspondingly, concerning the evolution of the production as a function of the mass loss, the simplified evaporation pattern (dashed line in Fig. 14) does not describe the measured descent of the mass-loss distribution in the range $\Delta A = 40$–70. The difference between the measured descent of the mass-loss distribution and the simplified evaporation calculation should correspond to the heavy fragments which are the partners of intermediate-mass fragments in asymmetric splits. It is possible that this explanation, already proposed for lighter systems such as ^{56}Fe$_{(1A\,\mathrm{GeV})}$+p [18], is rather general and describes also heavier systems at the energy range of 1 GeV per nucleon as, for instance, the system ^{208}Pb$_{(1A\,\mathrm{GeV})}$+p. The experimental cross sections of such systems [8] are presented in Fig. 14. The comparison of the two systems suggests that a similar intermediate-mass-fragment production could characterize also the system ^{208}Pb$_{(1A\,\mathrm{GeV})}$+p and increase the production cross section in the range $\Delta A = 40$–70, where the slope is almost identical for the two systems.

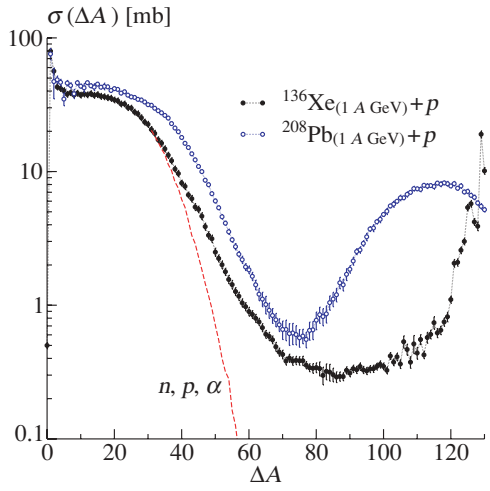

FIG. 14. (Color online) Mass-loss distribution of production cross sections. The experimental results obtained in the present work for the system ^{136}Xe$_{(1A\,\mathrm{GeV})}$+p are compared with the experimental results measured for the system ^{208}Pb$_{(1A\,\mathrm{GeV})}$+p [8] and with a calculation in which evaporation is limited to the emission of neutrons, protons, and α particles for ^{136}Xe$_{(1A\,\mathrm{GeV})}$+p (dashed line).

VI. CONCLUSIONS

The production cross sections of fully identified nuclides produced in the system ^{136}Xe$_{(1A\,\mathrm{GeV})}$+p were measured covering the element range from lithium to barium. The measurement of the kinetic energies imparted to the emitted residues completes the set of experimental data which is of high relevance both for applications, such as the radiation damage and activation of irradiated materials, and, more generally, for the modeling of spallation reactions.

The present measurement enables the first full survey of intermediate-mass-fragment cross sections measured together with heavy-fragment production in the decay of a neutron-rich system in the fissility region where asymmetric splits are predominant. The process of heavy-fragment formation in the system ^{136}Xe$_{(1A\,\mathrm{GeV})}$+p, determined mostly by sequential evaporation presents a phenomenology already observed in the decay of neutron-rich systems and establishes a direct

connection with the system $^{208}Pb_{(1A\,GeV)}+p$, measured in a former experiment [8]. The intermediate-mass-fragment production recalls the phenomenology observed in the system $^{56}Fe_{(1A\,GeV)}+p$, resumed by the U shape of the mass distribution and the very high kinetic energies which characterize the process [18]. These comparisons even suggest extending the description of the intermediate-mass-fragment formation, first proposed for light systems and confirmed in the present work for the decay of xenon, also to the heavier neutron-rich systems, in the fissility region where symmetric splits are largely more probable than asymmetric splits. As an extreme case, the light nuclide formation characterizing $^{238}U_{(1A\,GeV)}+p$ [14] may be explained by a similar scenario.

In this respect, the system $^{136}Xe_{(1A\,GeV)}+p$ is a representative system for studying the intermediate-mass-fragment formation in connection with the spallation process induced by protons in the 1*A* GeV energy range on neutron-rich targets; we propose it as a benchmark for testing the validity of models for spallation reactions over a large range of residue masses and charges. A correct identification of the process of formation of intermediate-mass fragments requires a dedicated analysis of the reaction kinematics and of the role of the Coulomb repulsion, as well as an exclusive measurement of correlation observables, and is a perspective for future research.

ACKNOWLEDGMENTS

We are particularly indebted to K. H. Behr, A. Brünle, and K. Burkard for their technical support in preparing and running the experiment. We wish to thank the group of P. Chesny, who conceived the liquid hydrogen target and checked its operation during the experiment. The participation of A.H. to this work has been supported by the U.S. DOE under Grant No. DE-FG02-91ER-40609.

[1] H. Geissel, P. Armbruster, K. H. Behr, A. Brünle, K. Burkard, M. Chen, H. Folger, B. Franczak, H. Keller, O. Klepper, B. Langenbeck, F. Nickel, E. Pfeng, M. Pfützner, E. Roeckl, K. Rykaczewski, I. Schall, D. Schardt, C. Scheidenberger, K.-H. Schmidt, A. Schroter, T. Schwab, K. Sümmerer, M. Weber, G. Münzenberg, T. Brohm, H.-G. Clerc, M. Fauerbach, J.-J. Gaimard, A. Grewe, E. Hanelt, B. Knödler, M. Steiner, B. Voss, J. Weckenmann, C. Ziegler, A. Magel, H. Wollnik, J. P. Dufour, Y. Fujita, D. J. Vieira, and B. Sherrill, Nucl. Instrum. Methods B **70**, 286 (1992).

[2] P. Chesny, A. Forges, J. M. Gheller, G. Guiller, P. Pariset, L. Tassan-Got, P. Armbruster, K. H. Behr, J. Benlliure, K. Burkard, A. Brünle, T. Enqvist, F. Farget, and K.-H. Schmidt, GSI 1997-1, p. 190 (unpublished).

[3] K-H. Schmidt, E. Hanelt, H. Geissel, G. Münzenberg, and J.-P. Dufour, Nucl. Instrum. Methods A **260**, 287 (1987).

[4] F. Rejmund, B. Mustapha, P. Armbruster, J. Benlliure, M. Bernas, A. Boudard, J. P. Dufour, T. Enqvist, R. Legrain, S. Leray, K.-H. Schmidt, C. Stéphan, J. Taïeb, L. Tassan-Got, and C. Volant, Nucl. Phys. **A683**, 540 (2001); B. Mustapha, Ph.D. thesis, IPN-Orsay, 1999.

[5] J. Benlliure, P. Armbruster, M. Bernas, A. Boudard, J. P. Dufour, T. Enqvist, R. Legrain, S. Leray, B. Mustapha, F. Rejmund, K.-H. Schmidt, C. Stéphan, L. Tassan-Got, and C. Volant, Nucl. Phys. **A683**, 513 (2001).

[6] B. Fernandez-Dominguez, P. Armbruster, L. Audouin, J. Benlliure, M. Bernas, A. Boudard, E. Casarejos, S. Czajkowski, J. E. Ducret, T. Enqvist, B. Jurado, R. Legrain, S. Leray, B. Mustapha, J. Pereira, M. Pravikoff, F. Rejmund, M. V. Ricciardi, K.-H. Schmidt, C. Stéphan, J. Taïeb, L. Tassan-Got, C. Volant, and W. Wlazlo, Nucl. Phys. **A747**, 227 (2005).

[7] L. Audouin, L. Tassan-Got, P. Armbruster, J. Benlliure, M. Bernas, A. Boudard, E. Casarejos, S. Czajkowski, T. Enqvist, B. Fernandez-Dominguez, B. Jurado, R. Legrain, S. Leray, B. Mustapha, J. Pereira, M. Pravikoff, F. Rejmund, M.-V. Ricciardi, K.-H. Schmidt, C. Stéphan, J. Taïeb, C. Volant, and W. Wlazlo, Nucl. Phys. **A768**, 1 (2006).

[8] T. Enqvist, W. Wlazlo, P. Armbruster, J. Benlliure, M. Bernas, A. Boudard, S. Czajkowski, R. Legrain, S. Leray, B. Mustapha, M. Pravikoff, F. Rejmund, K.-H. Schmidt, C. Stéphan, J. Taïeb, L. Tassan-Got, and C. Volant, Nucl. Phys. **A686**, 481 (2001).

[9] A. Kelic, K.-H. Schmidt, T. Enqvist, A. Boudard, P. Armbruster, J. Benlliure, M. Bernas, S. Czajkowski, R. Legrain, S. Leray, B. Mustapha, M. Pravikoff, F. Rejmund, C. Stéphan, J. Taïeb, L. Tassan-Got, C. Volant, and W. Wlazlo, Phys. Rev. C **70**, 064608 (2004).

[10] T. Enqvist, P. Armbruster, J. Benlliure, M. Bernas, A. Boudard, S. Czajkowski, R. Legrain, S. Leray, B. Mustapha, M. Pravikoff, F. Rejmund, K.-H. Schmidt, C. Stéphan, J. Taïeb, L. Tassan-Got, F. Vivès, C. Volant, and W. Wlazlo, Nucl. Phys. **A703**, 435 (2002).

[11] J. Taïeb, K.-H. Schmidt, L. Tassan-Got, P. Armbruster, J. Benlliure, M. Bernas, A. Boudard, E. Casarejos, S. Czajkowski, T. Enqvist, R. Legrain, S. Leray, B. Mustapha, M. Pravikoff, F. Rejmund, C. Stéphan, C. Volant, and W. Wlazlo, Nucl. Phys. **A724**, 413 (2003).

[12] M. Bernas, P. Armbruster, J. Benlliure, A. Boudard, E. Casarejos, S. Czajkowski, T. Enqvist, R. Legrain, S. Leray, B. Mustapha, P. Napolitani, J. Pereira, F. Rejmund, M. V. Ricciardi, K.-H. Schmidt, C. Stéphan, J. Taïeb, L. Tassan-Got, and C. Volant, Nucl. Phys. **A725**, 213 (2003).

[13] P. Armbruster, J. Benlliure, M. Bernas, A. Boudard, E. Casarejos, S. Czajkowski, T. Enqvist, S. Leray, P. Napolitani, J. Pereira, F. Rejmund, M.-V. Ricciardi, K.-H. Schmidt, C. Stéphan, J. Taïeb, L. Tassan-Got, and C. Volant, Phys. Rev. Lett. **93**, 212701 (2004).

[14] M. V. Ricciardi, P. Armbruster, J. Benlliure, M. Bernas, A. Boudard, S. Czajkowski, T. Enqvist, A. Kelic, S. Leray, R. Legrain, B. Mustapha, J. Pereira, F. Rejmund, K.-H. Schmidt, C. Stéphan, L. Tassan-Got, C. Volant, and O. Yordanov, Phys. Rev. C **73**, 014607 (2006).

[15] M. Bernas, P. Armbruster, J. Benlliure, A. Boudard, E. Casarejos, T. Enqvist, A. Kelic, R. Legrain, S. Leray, J. Pereira, F. Rejmund, M.-V. Ricciardi, K.-H. Schmidt, C. Stephan, J. Taïeb, L. Tassan-Got, and C. Volant, Nucl. Phys. **A765**, 197 (2006).

[16] E. Casarejos, J. Benlliure, J. Pereira, P. Armbruster, M. Bernas, A. Boudard, S. Czajkowski, T. Enqvist, R. Legrain, S. Leray, B. Mustapha, M. Pravikoff, F. Rejmund, K.-H. Schmidt, C. Stéphan, J. Taïeb, L. Tassan-Got, C. Volant,

and W. Wlazlo, Phys. Rev. C **74**, 044612 (2006).
[17] J. Pereira, J. Benlliure, E. Casarejos, P. Armbruster, M. Bernas, A. Boudard, S. Czajkowski, T. Enqvist, R. Legrain, S. Leray, B. Mustapha, M. Pravikoff, F. Rejmund, K.-H. Schmidt, C. Stéphan, J. Taïeb, L. Tassan-Got, C. Volant, and W. Wlazlo, Phys. Rev. C **75**, 014602 (2007).
[18] P. Napolitani, K.-H. Schmidt, A. S. Botvina, F. Rejmund, L. Tassan-Got, and C. Villagrasa, Phys. Rev. C **70**, 054607 (2004).
[19] C. Villagrasa-Canton, A. Boudard, J.-E. Ducret, B. Fernandez, S. Leray, C. Volant, P. Armbruster, T. Enqvist, F. Hammache, K. Helariutta, B. Jurado, M. V. Ricciardi, K.-H. Schmidt, K. Sümmerer, F. Vivès, O. Yordanov, L. Audouin, C.-O. Bacri, L. Ferrant, P. Napolitani, F. Rejmund, C. Stéphan, L. Tassan-Got, J. Benlliure, E. Casarejos, M. Fernandez-Ordonez, J. Pereira, S. Czajkowski, D. Karamanis, M. Pravikoff, J. S. George, R. A. Mewaldt, N. Yanasak, M. Wiedenbeck, J. J. Connell, T. Faestermann, A. Heinz, and A. Junghans, Phys. Rev. C **75**, 044603 (2007).
[20] U. L. Businaro and S. Gallone, Nuovo Cimento **1**, 629 (1955).
[21] U. L. Businaro and S. Gallone, Nuovo Cimento **1**, 1277 (1955).
[22] A. I. Warwick, A. Baden, H. H. Gutbrod, M. R. Maier, J. Péter, H. G. Ritter, H. Stelzer, H. H. Wieman, F. Weik, M. Freedman, D. J. Henderson, S. B. Kaufman, E. P. Steinberg, and B. D. Wilkins, Phys. Rev. Lett. **48**, 1719 (1982).
[23] A. I. Warwick, H. H. Wieman, H. H. Gutbrod, M. R. Maier, J. Péter, H. G. Ritter, H. Stelzer, F. Weik, M. Freedman, D. J. Henderson, S. B. Kaufman, E. P. Steinberg, and B. D. Wilkins, Phys. Rev. C **27**, 1083 (1983).
[24] A. S. Hirsch, A. Bujak, J. E. Finn, L. J. Gutay, R. W. Minich, N. T. Porile, R. P. Scharenberg, B. C. Stringfellow, and F. Turkot, Phys. Rev. C **29**, 508 (1984).
[25] L. N. Andronenko, A. A. Kotov, L. A. Vaishnene, W. Neubert, H. W. Barz, J. P. Bondorf, R. Donangelo, and H. Schulz, Phys. Lett. **B174**, 18 (1986).
[26] H. W. Barz, J. P. Bondorf, H. Schulz, L. N. Andronenko, A. A. Kotov, L. A. Vaishnene, and W. Neubert, Nucl. Phys. **A460**, 714 (1986).
[27] A. A. Kotov, L. N. Andronenko, M. N. Andronenko, Y. I. Gusev, K. V. Lukashin, W. Neubert, D. M. Seliverstov, I. I. Strakovsky, and L. A. Vaishnene, Nucl. Phys. **A583**, 575 (1995).
[28] W.-c. Hsi, K. Kwiatkowski, G. Wang, D. S. Bracken, E. Cornell, D. S. Ginger, V. E. Viola, N. R. Yoder, R. G. Korteling, F. Gimeno-Nogures, E. Ramakrishnan, D. Rowland, S. J. Yennello, M. J. Huang, W. G. Lynch, M. B. Tsang, H. Xi, Y. Y. Chu, S. Gushue, L. P. Remsberg, K. B. Morley, and H. Breuer, Phys. Rev. Lett. **79**, 817 (1997).
[29] S. P. Avdeyev, V. A. Karnaukhov, W. D. Kuznetsov, L. A. Petrov, V. K. Rodionov, A. S. Zubkevich, H. Oeschler, O. V. Bochkarev, L. V. Chulkov, E. A. Kuzmin, A. Budzanovski, W. Karcz, M. Janicki, E. Norbeck, A. S. Botvina, W. A. Friedman, W. Nörenberg, and G. Papp, Eur. Phys. J. A **3**, 75 (1998).
[30] A. S. Botvina, A. S. Iljinov, and I. N. Mishustin, JETP Lett. **42**, 572 (1985).
[31] W. G. Lynch, Annu. Rev. Nucl. Part. Sci. **37**, 493 (1987).
[32] A. S. Botvina, A. S. Iljinov, and I. N. Mishustin, Nucl. Phys. **A507**, 649 (1990).
[33] J. P. Bondorf, A. S. Botvina, A. S. Iljinov, I. N. Mishustin, and K. Sneppen, Phys. Rep. **257**, 133 (1995).
[34] V. A. Karnaukhov, S. P. Avdeyev, W. D. Kuznetsov, L. A. Petrov, V. K. Rodionov, A. S. Zubkevich, H. Oeschler, O. V. Bochkarev, L. V. Chulkov, E. A. Kuzmin, A. Budzanowski, W. Karcz, M. Janicki, E. Norbeck, and A. S. Botvina, Yad. Fiz. **62**, No. 2, 2272 (1999); Phys. At. Nucl. **62**, 237 (1999).
[35] L. G. Moretto, Nucl. Phys. **A247**, 211 (1975).
[36] L. G. Moretto and G. J. Wozniak, Pramana, J. Phys. **33**, 209 (1989).
[37] *Topical Volume: Dynamics and Thermodynamics with Nuclear Degrees of Freedom*, Eur. Phys. J. A **30** 1 (2006).
[38] V. E. Viola, K. Kwiatkowski, L. Beaulieu, D. S. Bracken, H. Breuer, J. Brzychczyk, R. T. de Souza, D. S. Ginger, W.-C. Hsi, R. G. Korteling, T. Lefort, W. G. Lynch, K. B. Morley, R. Legrain, L. Pienkowski, E. C. Pollacco, E. Renshaw, A. Ruangma, M. B. Tsang, C. Volant, G. Wang, S. J. Yennello, and N. R. Yoder, Phys. Rep. **434**, 1 (2006).
[39] H. Folger, H. Geissel, W. Hartmann, J. Klemm, G. Muenzenberg, D. Schardt, K.-H. Schmidt, and W. Thalheimer, Nucl. Instrum. Methods A **303**, 24 (1991).
[40] A. Junghans, H.-G. Clerc, A. Grewe, M. de Jong, J. Müller, and K.-H. Schmidt, Nucl. Instrum. Methods A **370**, 312 (1996).
[41] B. Jurado, K.-H. Schmidt, and K.-H. Behr, Nucl. Instrum. Methods A **483**, 603 (2002).
[42] K. Sümmerer (private communication).
[43] J. Benlliure, J. Pereira-Conca, and K.-H. Schmidt, Nucl. Instrum. Methods A **478**, 493 (2002).
[44] D. J. Morrissey, Phys. Rev. C **39**, 460 (1989).
[45] P. Napolitani *et al.* (in preparation).
[46] P. J. Karol, Phys. Rev. C **11**, 1203 (1975).
[47] T. Brohm, Ph.D. thesis, TH Darmstadt, 1994.
[48] J.-J. Gaimard and K.-H. Schmidt, Nucl. Phys. **A531**, 709 (1991).
[49] A. R. Junghans, M. de Jong, H.-G. Clerc, A. V. Ignatyuk, G. A. Kudyaev, and K.-H. Schmidt, Nucl. Phys. **A629**, 635 (1998).
[50] J. Benlliure, A. Grewe, M. de Jong, K.-H. Schmidt, and S. Zhdanov, Nucl. Phys. **A628**, 458 (1998).
[51] P. Napolitani, L. Tassan-Got, P. Armbruster, and M. Bernas, Nucl. Phys. **A727**, 120 (2003).
[52] B. L. Tracy, J. Chaumont, R. Klapisch, J. M. Nitschke, A. M. Poskanzer, E. Roeckl, and C. Thibault, Phys. Rev. C **5**, 222 (1972).
[53] M. V. Ricciardi, A. V. Ignatyuk, A. Kelic, P. Napolitani, F. Rejmund, K.-H. Schmidt, and O. Yordanov, Nucl. Phys. **A733**, 299 (2004).
[54] P. Napolitani, F. Rejmund, L. Tassan-Got, M. V. Ricciardi, A. Kelic, K.-H. Schmidt, O. Yordanov, A. V. Ignatyuk, and C. Villagrasa, Int. J. Mod. Phys. E **13**, 333 (2004).
[55] L. G. Moretto, Nucl. Phys. **A185**, 145 (1972).
[56] L. G. Moretto, Nucl. Phys. **A216**, 1 (1973).
[57] K.-H. Schmidt, M. V. Ricciardi, A. Botvina, and T. Enqvist, Nucl. Phys. **A710**, 157 (2002).
[58] J. P. Dufour, H. Delagrange, R. Del Moral, A. Fleury, F. Hubert, Y. Llabador, M. B. Mauhourat, K.-H. Schmidt, and A. Lleres, Nucl. Phys. **A387**, 157c (1982).
[59] R. J. Charity, Phys. Rev. C **58**, 1073 (1998).